Supporting Information for "Immediate-foreshocks indicating a common cascading earthquake rupture development"

Haoran Meng[1] **and Wenyuan Fan**[1]

[1]Scripps Institution of Oceanography, UC San Diego, La Jolla, CA 92093-0225, USA

Contents of this file

1. Texts S1 to S7
2. Caption for Table S1
3. References
4. Figures S1 to S11

Text S1. Second moments analysis

We perform empirical Green's function (eGf) analysis to obtain the apparent source time functions (ASTFs) for the M_w 5.4 earthquake. We obtain the ASTFs individually at each station by deconvolving seismograms of the M_w 5.4 event with those of a nearby M 3.7 earthquake to remove the path and site effects for both P- and S-waves (Figures S2). We use stations from the regional broadband networks and the strong motion networks to investigate the earthquake. The seismic records are band-pass filtered at 0.5 to 20.0 Hz with a causal 2nd-order Butterworth filter. The ASTFs show clearly separated episodes indicating two major subevents E1 and E2. The seismic moments of E1 and E2 are estimated by computing an average moment ratio between the two episodes and requiring the total moment equal to that of a M_w 5.4 earthquake. For each ASTF, a moment ratio is obtained from dividing the subevent moments, which are integrations of the episodes respectively (Figure S2a). The moment ratio of E1 to E2 is about 5%, equivalent to a M_w 4.5 earthquake for E1. We further estimate the centroid location separation distance by curve fitting the centroid lag time at different directions (Figures 1b and S2). The centroid location of E2 is 1.1 km northeast of E1, showing that the earthquake ruptured a fault plane that is orthogonal to the main fault strike of the M_w7.1 mianshock (Shelly, 2020).

With the ASTFs and a local 1D velocity model, we solve the rupture length and width of the subevent E2 by estimating its second seismic moments. The 1D velocity model is obtained from averaging the community velocity model of Southern California (Lee et al., 2014). We closely follow a method that is used to study the second moments of other Southern California earthquakes (Meng et al., 2020; McGuire, 2004, 2017), and only briefly explain the physical meanings of the second moments here. Centroid location and centroid time are the first moments of an earthquake, and the second seismic moments characterize the variances of the first moments, which effectively represent the earthquake length, width, duration and rupture directivity (Backus & Mulcahy, 1976a, 1976b; McGuire, 2004). Knowing the local velocity structure, the second seismic moments $\underline{\underline{\widehat{\mu}}}^{(2,0)}$, $\widehat{\mu}^{(0,2)}$, and $\underline{\widehat{\mu}}^{(1,1)}$ can be obtained by solving:

$$\widehat{\mu}^{(0,2)}(\underline{s}) = \widehat{\mu}^{(0,2)} - 2\underline{s} \cdot \widehat{\mu}^{(1,1)} + \underline{s} \cdot \underline{\underline{\widehat{\mu}}}^{(2,0)} \underline{s} \tag{1}$$

where $\widehat{\mu}^{(0,2)}(\underline{s})$ is the apparent duration obtained from the ASTF and $\underline{s}$ is the slowness of either P- or S-waves in the source region for a given source-receiver pair (McGuire, 2004). The second moments can estimate an earthquake characteristic duration ($\tau_c = 2\sqrt{\widehat{\mu}^{(0,2)}}$) and earthquake characteristic rupture extents ($x_c(\underline{\widehat{n}}) = 2\sqrt{\underline{\widehat{n}}^T \underline{\underline{\widehat{\mu}}}^{(2,0)} \underline{\widehat{n}}}$), where $\underline{\widehat{n}}$ is a unit eigenvector of $\underline{\underline{\widehat{\mu}}}^{(2,0)}$ and x_c represents the associated rupture dimension, e.g., the rupture length L_c or the rupture width W_c (McGuire, 2004).

Following a case study of the 1999 Izmit, Turkey M_w 7.6 earthquake and its foreshocks (Ellsworth, 2019), we estimate the stress perturbations from E1 to E2. We approximate the subevent E1 as a M_w 4.5 earthquake (point source) with the same focal mechanism of the M_w 5.4 earthquake, and assume the E1 source time function as a parabola function lasting 0.3 s. We then synthesize a 3D displacement field of E1 in a whole-space homogeneous medium with $V_p = 6.169$ km/s, $V_s = 3.523$ km/s, and $\rho = 2,600$ kg/m^3 (Aki & Richards, 2002) (Figure S3). The 3D model space is set as 4,000 m along strike by 4,000 m along dip by 40 m perpendicular to the fault surface with a grid spacing of 20 m and the subevent E1 is set in the center of the model space. We calculate the three-component displacements at each grid for 2 seconds with a sampling rate of 500 Hz to account for both the transient- and permanent-displacement. The strain-tensor perturbations on the fault plane are computed as numerical spatial derivatives of the displacement field. We then use the Hooke's law to obtain the stress perturbations. The fault-plane normal stress perturbations are zero and the static and peak dynamic shear stress perturbations exceed 0.1 MPa in the vicinity of the subevent E2 (Figures 2 and S3).

Text S2. Detection of immediate-foreshocks

We detect immediate-foreshocks by using the vertical component records and autocorrelating the P-waves with their 100 s preceding waveforms. The seismic records are band-pass filtered at 1 to 20 Hz with a causal 2nd-order Butterworth filter. With a regional catalog (SCEDC; Hutton et al., 2010), the P-wave arrival times are first calculated using a 1D velocity model, which is obtained from averaging the community velocity model of Southern California (Lee et al., 2014). The P-wave onset times are then further refined with manual corrections. The autocorrelation is performed independently for all stations within epicentral distance of 30 km, including both the regional network stations, the rapid deployment broadband stations, and the nodal array stations. For a given station, we test a set of P-wave time windows from 0.5 s to 1.0 s with an incremental step of 0.1 s, and the preferred time window of the event-station pair maximizes the autocorrelation coefficient (AC).

For a given event, we select candidate stations with maximum AC greater than 0.7, and record the autocorrelation differential time (signal preceding time) and the amplitude ratio in addition to the autocorrelation coefficient. For $M \leq 3.5$ earthquakes, an immediate-foreshock is detected when (1), the average AC exceeds 0.8 for more than 10 stations; (2), these stations are from an azimuthal range greater than 180°; (3), the preceding time distribution has a standard deviation less than 0.01 s. For $3.5 \leq M \leq 5.0$ earthquakes (there are only 3 events), we impose a similar set of criteria, including (1), the average AC exceeds 0.7 for more than 10 stations; (2), these stations are from an azimuthal range greater than 180°; (3), the preceding time distribution has a standard deviation that is less than 0.05 s. P-waves are more complex for larger magnitude earthquakes, and this modification allows us to effectively search immediate-foreshocks for all earthquakes with $0.5 \leq M \leq 5.4$. In total, we find 527 earthquakes with clear immediate-foreshocks and do not observe a magnitude dependence of the measured amplitude ratio or the preceding time.

The three-component nodal stations are short-period seismographs with a natural frequency of 5 Hz. Because of the natural frequency, the instruments may fail to record the low frequency (≤5 Hz) ground motion faithfully. Additionally, the band-pass filter (1-20 Hz) used in the analysis may introduce possible biases. To evaluate these potential biases, we compare the records of four earthquakes from M 2.5 to M 4.0 at a pair of collocated seismographs, including a broadband station CA03 and a nodal station U01 (Figure S11). We first remove the instrumental responses and then band-pass filter the records at 0.2 to 45 Hz with a causal 2nd-order Butterworth filter. The two sensors recorded almost identical ground motions and the results show that the nodal stations can record the investigated earthquakes with high fidelity. Given the noise level and the site conditions of the nodal stations, the 1-20 Hz band-pass filter can effectively suppress the high-frequency noise, and it does not impact small earthquake amplitudes very much. Our results show that the nodal array stations recorded high-quality data, and they can be used to investigate a range of earthquake rupture features.

Text S3. Estimating the creeping transition depth

Following the standard approach (Magistrale, 2002; Rolandone et al., 2004), we estimate the deep creeping transition depth as the 95 percent earthquake depth threshold. In this study, the seismogenic zone depth extent is estimated as 11.0 km from a regional catalog of the 2019 Ridgecrest sequence (SCEDC; Hutton et al., 2010).

Text S4. Relative location of the immediate-foreshocks

We determine the relative locations between the immediate-foreshocks and the mainshocks using the differential times measured at multiple seismic stations. We first compute the slowness of the P-wave in the source region with a 1D velocity model, which is obtained from averaging the community velocity model of Southern California (Lee

et al., 2014). The preceding time t_j of the precursory signal from an immediate-foreshock i at station j and the location of the immediate-foreshock are linked as

$$t_j = \Delta \underline{r}_i \cdot \underline{s}_{ij} + t_{0j} \tag{2}$$

where $\Delta \underline{r}_i$ is the relative location between the ith pair of the immediate-foreshock and the mainshock, $\underline{s}_{ij}$ is the slowness vector of P-wave in the source region of the seismic ray-path connecting the mainshock hypocenter and the seismograph j, and t_{0j} is the preceding time of the immediate-foreshock. With multiple measurements of t_j, the relative location and preceding origin time can be determined using the equation above. With the relative locations, we found most of these foreshocks are located within 0.2 km of their mainshocks with a median separation of 59 m (Figure 4a).

We further evaluate the uncertainties of the relative locations by performing jackknife-resampling of the stations (Efron & Tibshirani, 1994). For each realization, we remove one measurement t_j and perform inversion with the remaining measurements. For a given separation distance (e.g., the vertical separation distance) or origin time m, $\hat{m}_j$ is the jth jackknife realization of m and $\hat{m}$ is the mean of $\hat{m}_j$:

$$\hat{m} = \frac{1}{N} \sum_{i=1}^{N} \hat{m}_j \tag{3}$$

where N is the total number of measurements. The jackknife estimate of the standard deviation ($\hat{m}_\sigma$) of m is computed as

$$\hat{m}_\sigma = \sqrt{\frac{N-1}{N} \sum_{i=1}^{N} (\hat{m}_j - \hat{m})^2} \tag{4}$$

We estimate the standard deviations (uncertainties) at three directions independently for the hypocentral separations of the 527 immediate-foreshock and the mainshock pairs (Figure S7). About 85% of the separation distance between the immediate-foreshocks and mainshocks has a standard deviation less than 0.1 km with a median value of 15 m horizontally (Figure S7f). Vertically, 78% of the separation distance has a standard deviation less than 0.1 km with a median value of 31 m (Figure S7f).

Text S5. Foreshock-mainshock and mainshock-aftershock sequences in a local high resolution catalog

We use a catalog that is obtained with a template matching technique (Shelly, 2020) to investigate the foreshock-mainshock and mainshock-aftershock sequences of the Ridgecrest earthquakes. The high resolution catalog reports 34,091 $-0.3 \leq M \leq 7.1$ earthquakes occurring from 4 July 2019 to 16 July 2019 in the Ridgecrest region (Shelly, 2020). For a given earthquake, we search for events preceding the target earthquake within 100 s and within 1 km hypocentral distance. If these events have magnitudes smaller than the target earthquake, they are considered as foreshocks of the target earthquake. In total, there are 524 candidate foreshock-mainshock sequences with one or more foreshocks. Out of the 524 candidates, 363 foreshock-mainshock sequences are further confirmed by visual inspections of the nodal array waveforms, and we focus on analyzing these cases. Out of the 363 earthquakes, 16 events have more than one foreshocks and the remaining earthquakes only have a single foreshock. There are no clear migration patterns of the foreshock-mainshock sequences. The preceding time, magnitude, hypocentral separation and depth of these foreshocks show similar characteristics to the 527 immediate-foreshocks reported in this study (Figures S8 and 3). We also search for earthquakes with smaller magnitudes within 100 s after a target earthquake and within 1 km hypocentral distance. These events are considered aftershocks. In total, we find 519 mainshock-aftershock sequences in Shelly (2020).

Text S6. Inverse Omori's law

We evaluate the frequencies of the 527 immediate-foreshocks reported in this study and the 363 foreshocks in Shelly (2020). The seismicity rate is evaluated by binning the event occurrence in 5 seconds non-overlapping bins up to 100 seconds preceding the main events (Figure S9). Both the immediate-foreshocks and the foreshocks occur more frequently as the mainshock approaches, following an exponential increase trend. Assuming such increases follow an inverse Omori's law, $k/(-t)^p$, where k is a productivity constant and p is the growing rate, we perform a grid search on these two parameters to fit the two parameters for both catalogs respectively. We found a growing rate of $p = 0.57$ for the 527 immediate-foreshocks and a rate of $p = 0.89$ for the 363 foreshocks in the Shelly (2020) catalog. The the different p-values may indicate a possible difference in triggering efficiency at different scales (Figure 4). However, the physical meaning of the p parameter is unclear and we do not discuss the details in this paper (Shcherbakov et al., 2004).

Text S7. Data and materials

The earthquake catalogs were accessed from Southern California Earthquake Data Center (SCEDC; Hutton et al., 2010) and Shelly (2020). The seismic data were provided by Data Management Center (DMC) of the Incorporated Research Institutions for Seismology (IRIS) and the SCEDC (Caltech.Dataset., 2013). The facilities of IRIS Data Services, and specifically the IRIS Data Management Center, were used for access to waveforms, related metadata, and/or derived products used in this study. IRIS Data Services are funded through the Seismological Facilities for the Advancement of Geoscience and EarthScope (SAGE) Proposal of the National Science Foundation (NSF) under Cooperative Agreement EAR-1261681. The nodal array data is openly available through IRIS DMC and was acquired by the U.S. Geological Survey (USGS) (Catchings et al., 2020) and the Southern California Earthquake Center (SCEC) and SCEC member institutions. The experiments were led by Rufus D. Catchings and Mark R. Goldman. The rapid seismic deployment of nodes for the 2019 Ridgecrest earthquake sequence was partially supported by the U.S. Geological Survey (USGS), the Southern California Earthquake Center, and the National Science Foundation (Grant Number EAR-1945781).

Table 1. 527 earthquakes with immediate-foreshocks. The event ID and locations are from the SCEDC catalog (Hutton et al., 2010).

References

Aki, K. (1965). Maximum likelihood estimate of b in the formula log n= a-bm and its confidence limits. *Bull. Earthq. Res. Inst., Tokyo Univ.*, *43*, 237–239.

Aki, K., & Richards, P. G. (2002). *Quantitative seismology.*

Backus, G., & Mulcahy, M. (1976a). Moment tensors and other phenomenological descriptions of seismic sources–I. continuous displacements. *Geophysical Journal International*, *46*(2), 341–361. doi: 10.1111/j.1365-246x.1976.tb04162.x

Backus, G., & Mulcahy, M. (1976b). Moment tensors and other phenomenological descriptions of seismic sources–II. discontinuous displacements. *Geophysical Journal International*, *47*(2), 301–329. doi: 10.1111/j.1365-246x.1976.tb01275.x

Caltech.Dataset. (2013). Southern California Earthquake Data Center. doi: 10.7909/C3WD3xH1

Catchings, R. D., Goldman, M., Steidl, J., Chan, J., Allam, A., Criley, C., ... Ben-Zion, Y. (2020). Nodal seismograph recordings of the 2019 Ridgecrest earthquake sequence. *Seismological Research Letters*, *91*(6), 3622—3633.

Efron, B., & Tibshirani, R. J. (1994). *An introduction to the bootstrap.* CRC press.

Ellsworth, W. L. (2019). From foreshocks to mainshocks: mechanisms and implications for earthquake nucleation and rupture propagation. *Mechanics of Earthquake Faulting*, *202*, 95.

Hutton, K., Woessner, J., & Hauksson, E. (2010). Earthquake monitoring in southern california for seventy-seven years (1932–2008). *Bulletin of the Seismological Society of America*, *100*(2), 423–446.

Lee, E.-J., Chen, P., Jordan, T. H., Maechling, P. B., Denolle, M. A., & Beroza, G. C. (2014). Full-3-D tomography for crustal structure in southern California based on the scattering-integral and the adjoint-wavefield methods. *Journal of Geophysical Research: Solid Earth*, *119*(8), 6421–6451.

Magistrale, H. (2002). Relative contributions of crustal temperature and composition to controlling the depth of earthquakes in southern California. *Geophysical research letters*, *29*(10), 87–1.

McGuire, J. J. (2004). Estimating finite source properties of small earthquake ruptures. *Bulletin of the Seismological Society of America*, *94*(2), 377–393. doi: 10.1785/0120030091

McGuire, J. J. (2017). A MATLAB toolbox for estimating the second moments of earthquake ruptures. *Seismological Research Letters*, *88*(2A), 371–378. doi: 10.1785/0220160170

Meng, H., McGuire, J. J., & Ben-Zion, Y. (2020). Semiautomated estimates of directivity and related source properties of small to moderate southern California earthquakes using second seismic moments. *Journal of Geophysical Research: Solid Earth*, *125*(4), e2019JB018566.

Rolandone, F., Bürgmann, R., & Nadeau, R. (2004). The evolution of the seismic-aseismic transition during the earthquake cycle: constraints from the time-dependent depth distribution of aftershocks. *Geophysical Research Letters*, *31*(23).

Shcherbakov, R., Turcotte, D. L., & Rundle, J. B. (2004). A generalized omori's law for earthquake aftershock decay. *Geophysical research letters*, *31*(11).

Shelly, D. R. (2020). A high-resolution seismic catalog for the initial 2019 Ridgecrest earthquake sequence: foreshocks, aftershocks, and faulting complexity. *Seismological Research Letters*, *91*(4), 1971—1978.

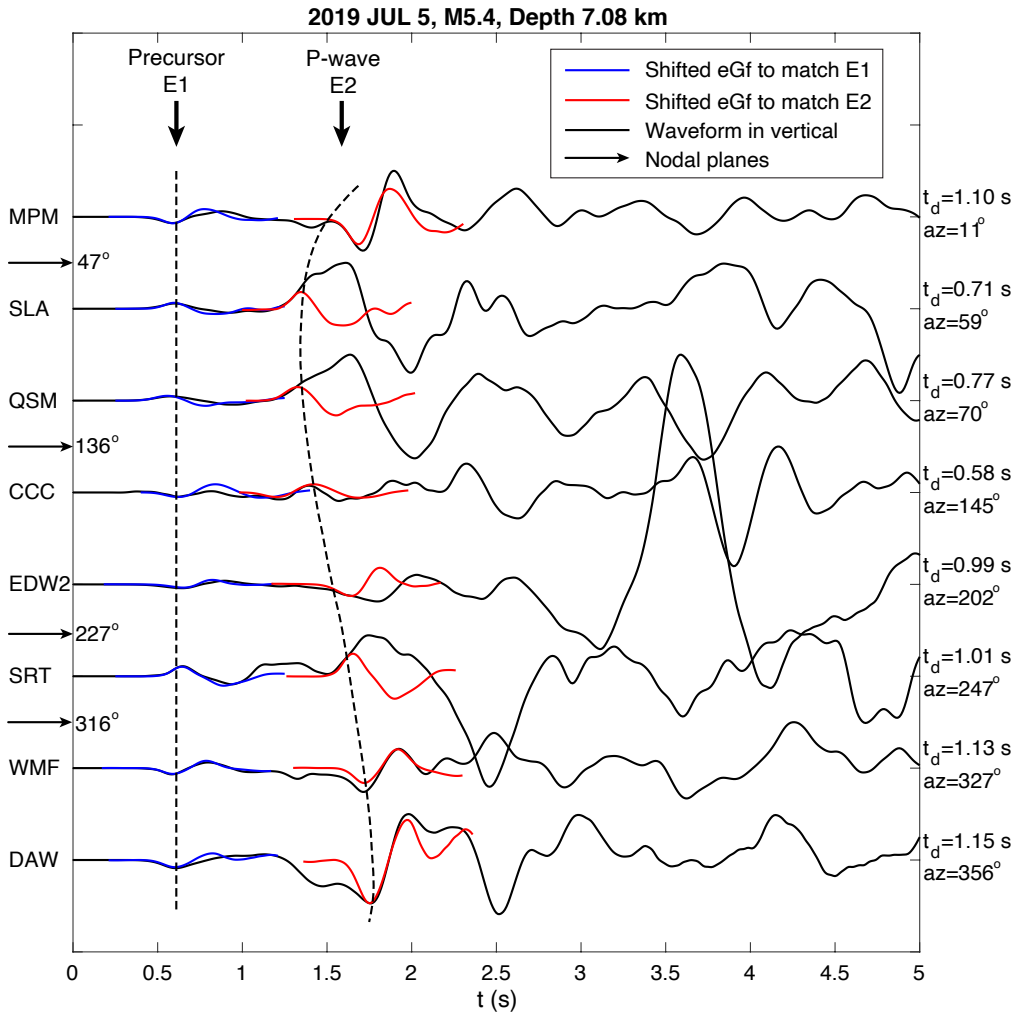

Figure S1. Precursory signals and P-waves of the M_w 5.4 earthquake at eight example broadband stations. The waveforms are from the vertical-component records and are band-pass filtered at 0.2 to 20 Hz with a causal 2nd-order Butterworth filter. The traces are aligned with their station azimuths. The station names and azimuthal directions are listed by the traces. az stands for the azimuth and t_d is the preceding time. The blue and red curves are scaled P-waves of a nearby M 3.7 eGf. Arrows show the nodal plane directions of the M_w 5.4 earthquake. The black dash-curves show the arrival times of the two subevents E1 and E2 with the first event aligned at 0.6 seconds. The differential arrival times suggest a northeast rupture propagation.

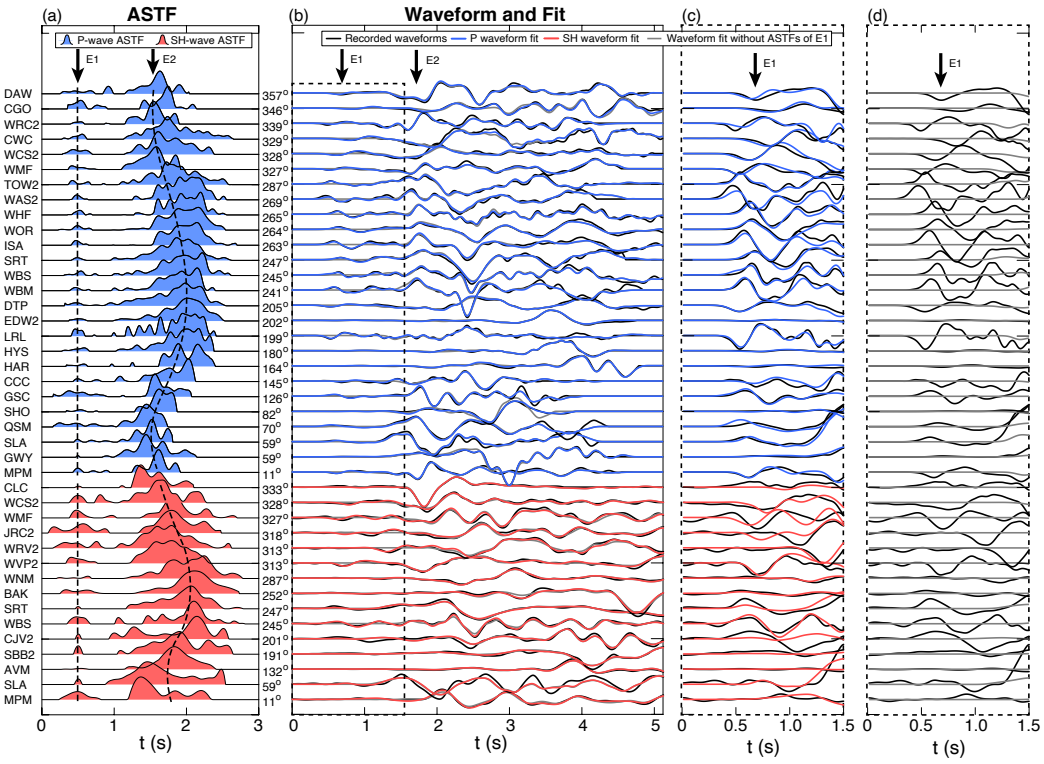

Figure S2. The apparent source time functions (ASTFs) and the waveform fit of the M_w 5.4 earthquake. (a) The ASTFs of P-waves (blue) and SH-waves (red). The black dash-curves show the centroid lag times at different stations (see Figure 2). The early small pulses are the ASTFs of subevent E1 and the later strong pulses are the ASTFs of subevent E2. (b) Waveforms of the observed and synthesized P- and SH-waves. The black traces are observations recorded by regional broadband and strong motion seismographs, the blue traces are synthetic P-waves, and the red traces are synthetic SH-waves. The gray traces are the synthetic waveforms by suppressing the ASTFs of E1. (c) and (d) The zoomed-in view of the waveforms and synthetics of E1. The observations cannot be recovered by the synthetics without the ASTFs of E1.

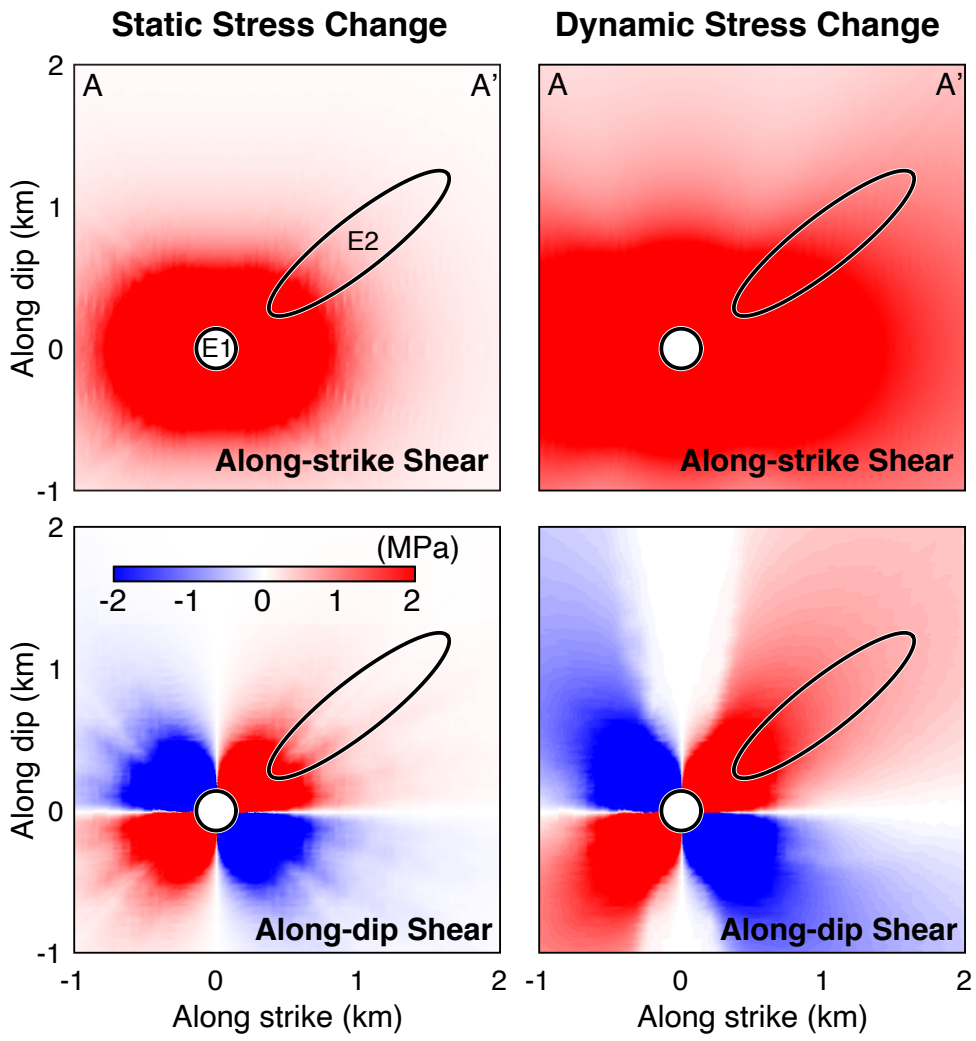

Figure S3. Static and peak dynamic shear stress perturbations from E1 to E2 of the M_w 5.4 earthquake on a 42°-strike fault plane. The static and dynamic normal stress changes are zero.

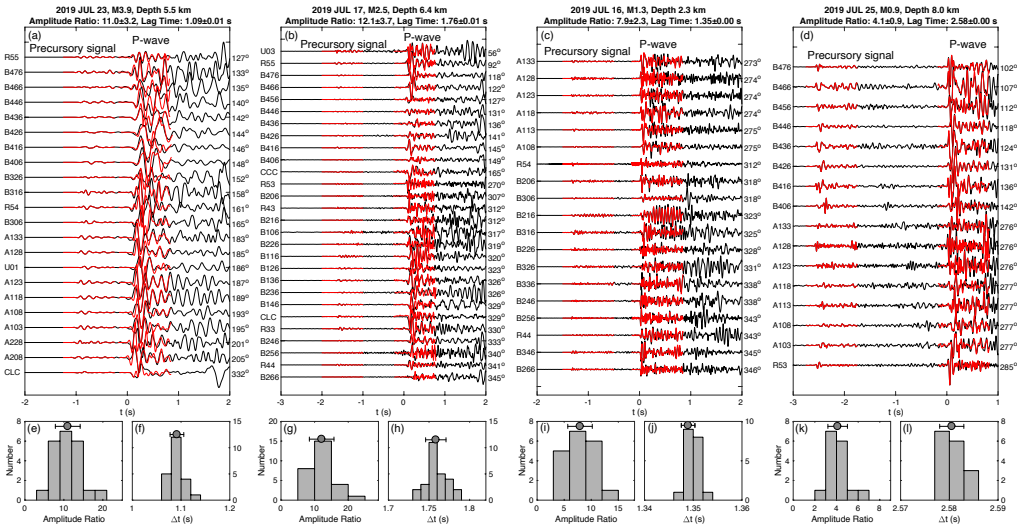

Figure S4. (a) Precursory signals and P-waves of a M 3.9 earthquake (Figure 2). The earthquake event ID is 38627095 (35.74567°/−117.55800°/5.5 km). (b) Precursory signals and P-waves of a M 2.5 earthquake. The earthquake event ID is 38592095 (35.64167°/ − 117.47150°/6.4 km). (c) Precursory signals and P-waves of a M 1.3 earthquake. The earthquake event ID is 38580791 (35.61883°/ − 117.46617°/2.3 km). (d) Precursory signals and P-waves of a M 0.9 earthquake. The earthquake event ID is 38641623 (35.60983°/ − 117.45650°/8.0 km) (SCEDC; Hutton et al., 2010). The waveforms are recorded by the nodal array stations and they are band-pass filtered at 1 to 20 Hz with a causal 2nd-order Butterworth filter. The station names and station azimuths (az) are listed by the traces. (e) to (l) The corresponding amplitude ratio and preceding time (Δt) distributions of (a) to (d). The gray circle and error-bar show the mean and one standard deviation of the amplitude ratio or the preceding time.

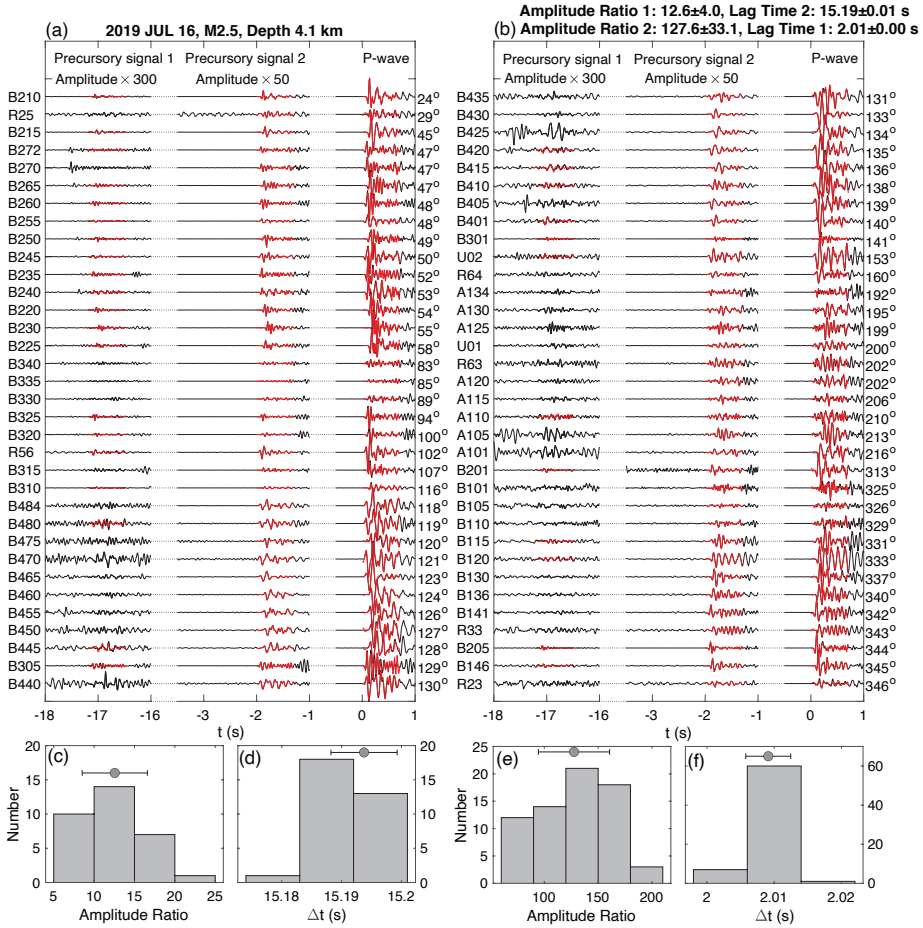

Figure S5. (a) and (b) Successive precursory signals and P-waves of a M 2.5 earthquake. The earthquake event ID is 38582951 (35.68017°/ − 117.54300°/4.1 km) (SCEDC; Hutton et al., 2010). The waveforms are recorded by the nodal array stations and are band-pass filtered at 1 to 20 Hz. (c) and (d) Corresponding amplitude ratio and preceding time distributions of precursory signals 1 and 2. (e) and (f) Corresponding amplitude ratio and preceding time distributions of precursory signal 2 and P-wave. The gray circles and error-bars show the mean and one standard deviation of the amplitude ratio or the preceding time.

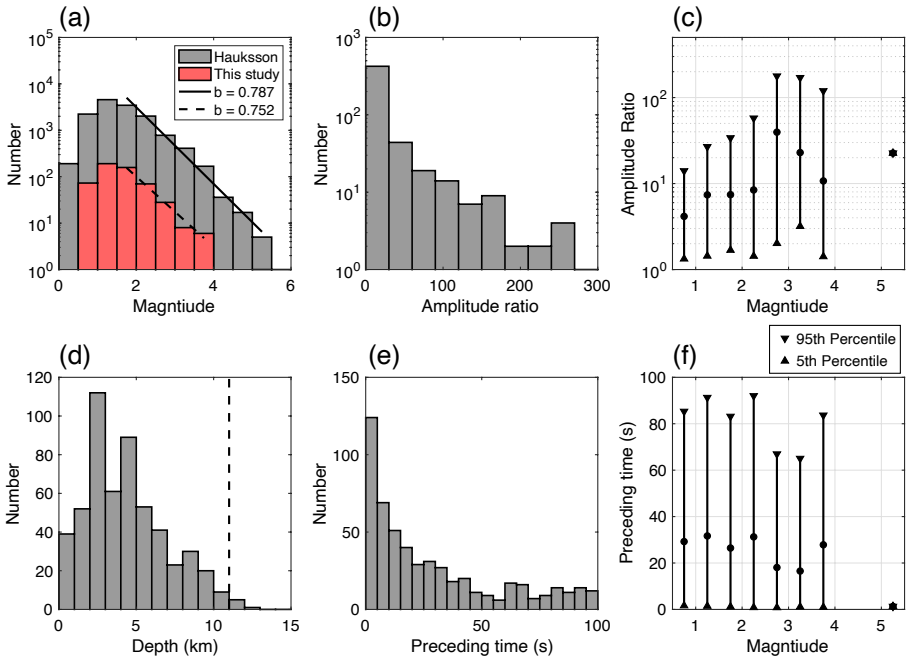

Figure S6. (a) The magnitude-frequency distribution of the 13,895 analyzed earthquakes and 527 events with observed immediate-foreshocks. (b), (d) and (e) The distributions of amplitude ratio, depth, and preceding times of the 527 events with observed immediate-foreshocks. The magnitude-frequency distribution of the earthquakes with immediate-foreshocks is statistically similar to that of the investigated earthquakes. The solid and dashed black lines in (a) show b-values of all analyzed earthquakes and events with immediate-foreshocks 0.787 and 0.752 respectively (Aki, 1965). We use earthquakes with magnitudes from 1.5 to 5.5 to estimate the b-values. (c) and (f) The range of the amplitude ratio and the preceding time of earthquakes with different magnitudes. Earthquakes are binned with a 0.5 magnitude interval from 0.5 to 5.5. The bars show 5 and 95 percentiles of the measurable. The dashed line is the 95 percentile seismicity depth, 11.0 km (Text S3).

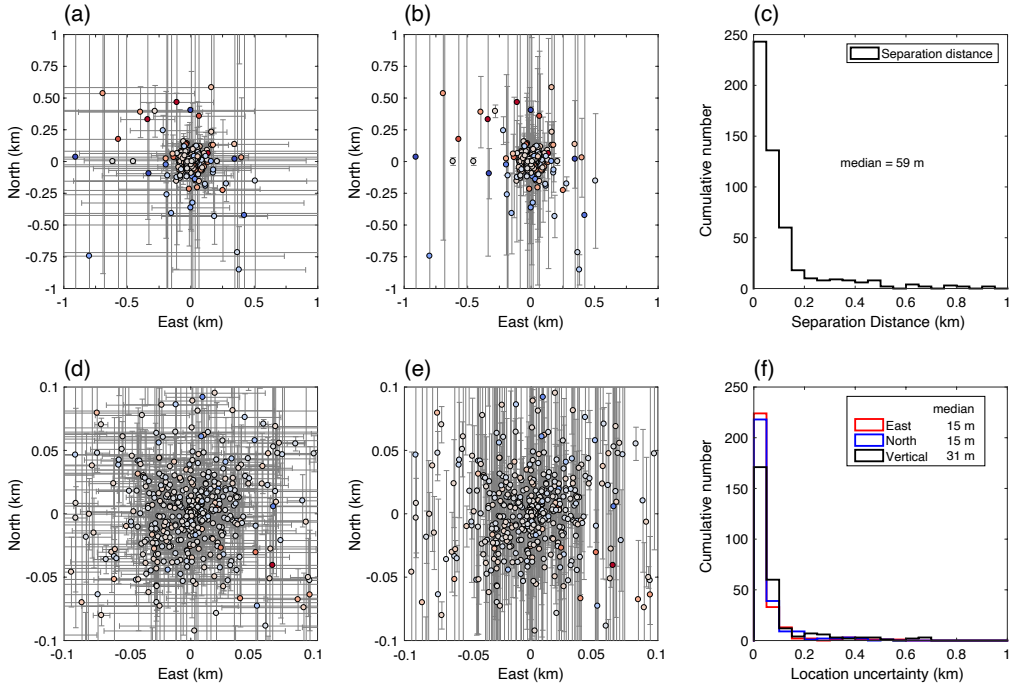

Figure S7. (a) Horizontal and vertical the separations of the immediate-foreshocks to the mainshocks. The error bars show the location uncertainties in the east and north component estimated using jackknife-resampling method (Text S4). (b) Similar to (a), but with the error bars showing the location uncertainties in the vertical component. (c) A histogram of the hypocentral separations between the immediate-foreshocks and the mainshocks. (d) and (e) The zoomed-in views of (a) and (b). (f) The histograms of location uncertainties in east, north, and vertical component.

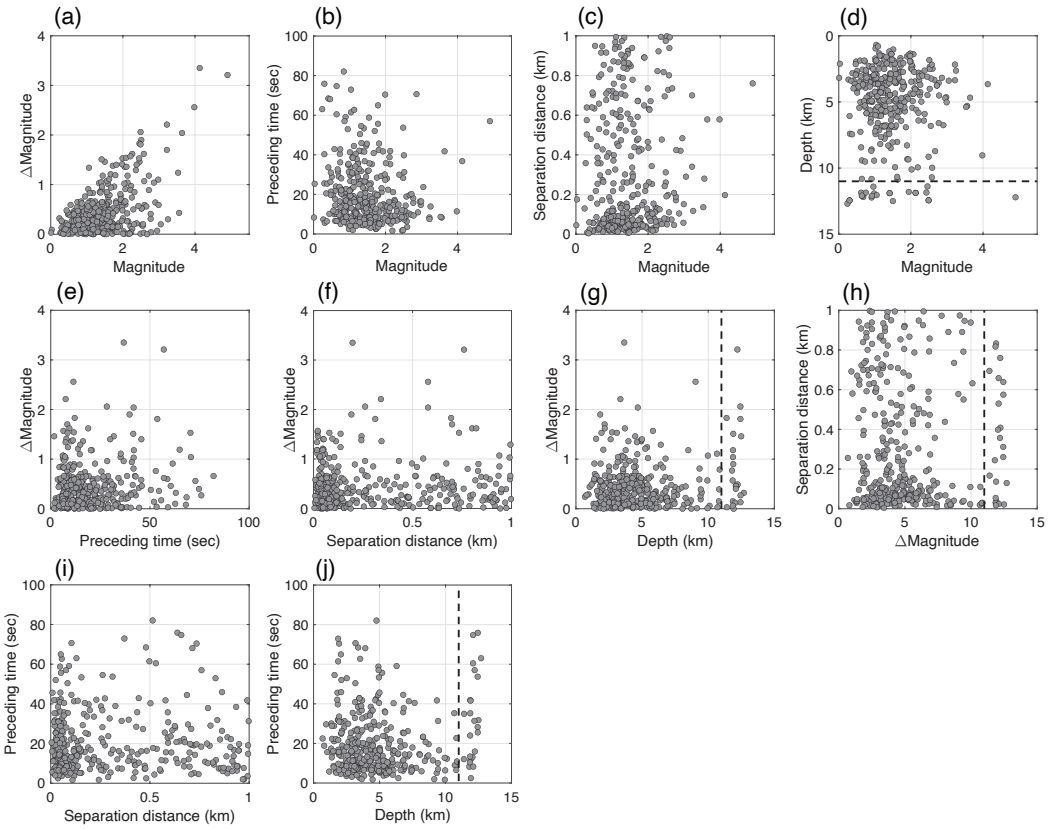

Figure S8. Scatter plots of the differential magnitude, preceding time, magnitude, hypocentral separation, and depth of the 363 foreshock-mainshock sequences in a local high-resolution catalog (Shelly, 2020). The dashed line is the 95 percentile seismicity depth, 11.0 km (Text S3).

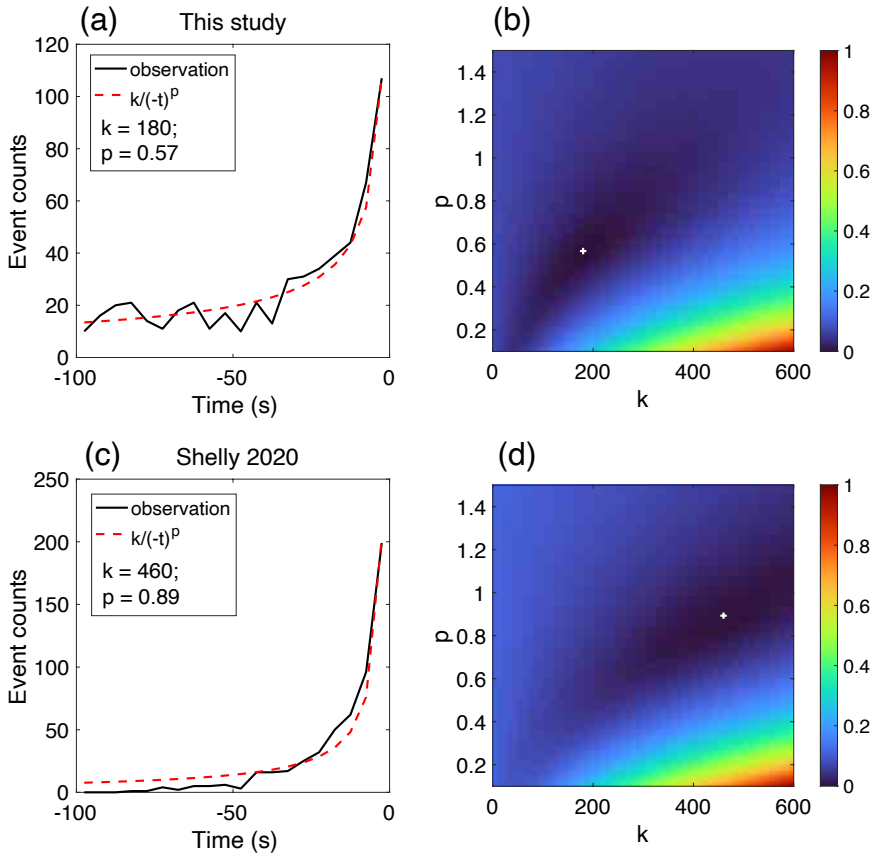

Figure S9. Event occurrence and inverse Omori law fits. (a) Differential time distribution of the immediate-foreshocks detected in this study and the inverse Omori law fit. (b) Normalized residuals by performing grid search on k and p, $p = 0.57$ for the best fit. (c) Differential time distribution of foreshocks in Shelly (2020) and the inverse Omori law fit. The foreshocks are selected with preceding time less than 100 seconds and spatial separation less than 1 km of the mainshocks. (c) Normalized residuals by performing grid search on k and p, $p = 0.89$ for the best fit.

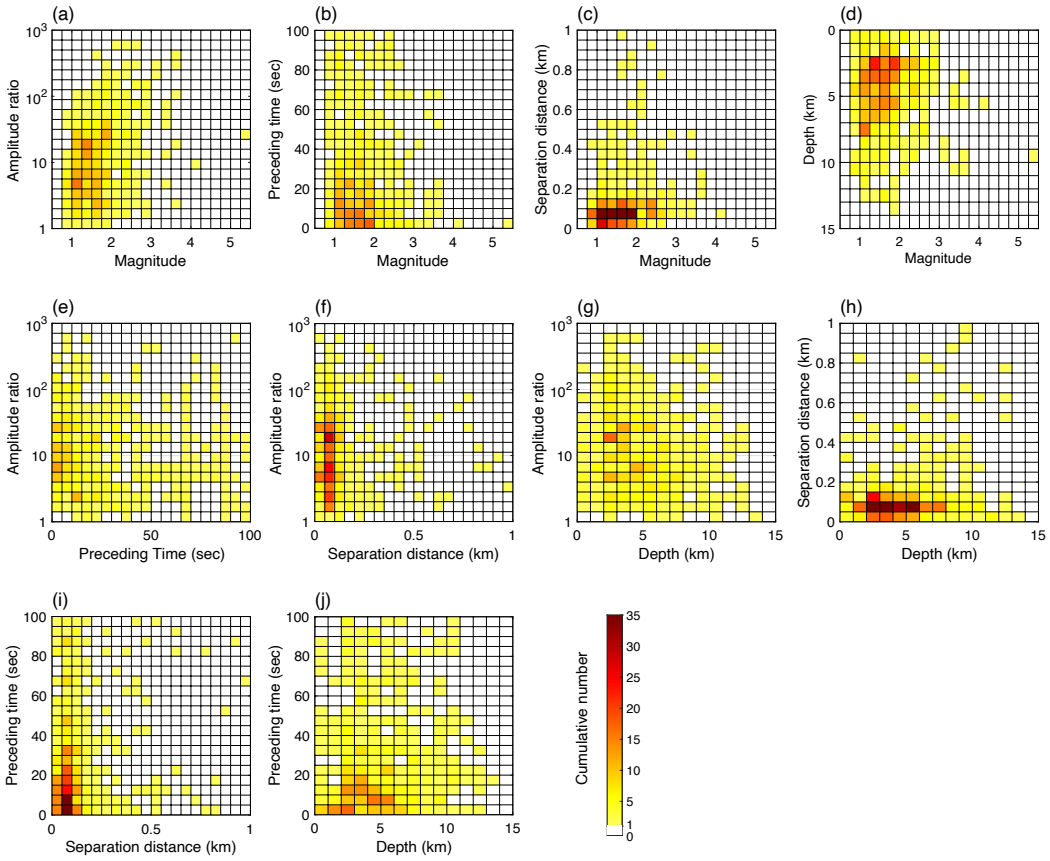

Figure S10. Earthquake density plots of the measured amplitude ratio, preceding time, magnitude, hypocentral separation, and depth of the 527 earthquakes with their observed immediate-foreshocks.

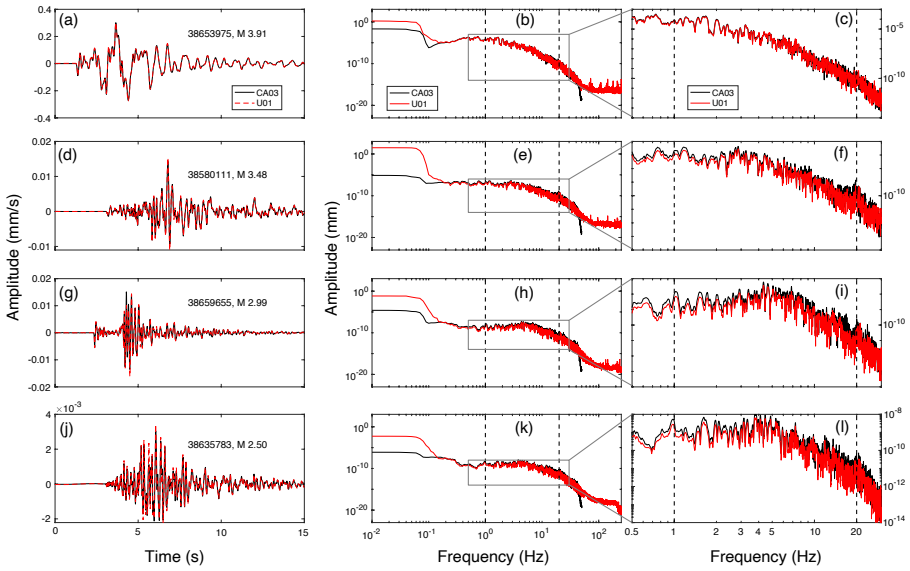

Figure S11. Ground motion comparison of two collocated seismographs. (a) Vertical-component velocity-waveforms of a M 3.9 earthquake at the nodal station U01 and the broad-band station CA03. The earthquake event ID is 38653975 (35.63717°/ − 117.47417°/1.6 km). (b) Velocity spectra of the raw waveforms of the M 3.9 event at the collocated stations. The instrumental responses are removed. (c) A zoomed-in view of the gray box in (b). (d) to (l) The waveform and spectrum comparisons for a M 3.5 earthquake (ID: 38580111, 35.59900°/ − 117.37100°/5.7 km), a M 3.0 earthquake (ID: 38659655, 35.68417°/ − 117.52483°/9.2 km), and a M 2.5 earthquake (ID: 38635783, 35.59617°/ − 117.43250°/6.4 km). The waveforms are band-pass filtered at 0.2 to 45.0 Hz with a causal 2nd-order Butterworth filter. The event IDs and locations are from the SCEDC catalog (Hutton et al., 2010).